VIII International Conference on Particle-Based Methods
PARTICLES 2023
U. Perego, M. Cremonesi, A. Franci (Eds)

COMPARATIVE ANALYSIS OF SOFTENING CONTACT LAWS IN PARTICLE MODELS: APPLICATION TO ROCK AND CONCRETE

N. MONTEIRO AZEVEDO[*1], M.L. BRAGA FARINHA[*2] AND S. OLIVEIRA[*3]

[*]Concrete Dams Department
Laboratório Nacional de Engenharia Civil (LNEC)
Av. do Brasil 101, 1700-066 Lisboa, Portugal
e-mail: [1]nazevedo@lnec.pt, [2]lbraga@lnec.pt, [3]soliveira@lnec.pt, www.lnec.pt/barragens-betao

Abstract. In this work three constitutive contact models that include softening are adopted for particle model fracture studies in both rock and concrete. For a single local contact, the constitutive contact model performance is initially compared in tensile, pure shear and shear tests under constant axial. Additionally, compression, direct tensile, and confined triaxial tests of quasi-britlle material discretized with spherical particles are presented and the predicted macroscopic response is compared. For a single local contact, the three contact models predict a similar behaviour. As shown, it is possible to calibrate each contact model to reproduce complex macroscopic behaviour observed in rock and concrete, but each contact model requires different contact properties or particle generation procedures.

Keywords: Particle modelling, Discrete element, Contact laws, Fracture, Rock, Concrete.

1 INTRODUCTION

Nowadays it is possible to predict, evaluate and understand cracking phenomena in quasi-brittle materials through numerical models, among them detailed rigid particle models (PM) that take directly into consideration the physical mechanisms and the influence of the material grain structure. These models have gained relevance in rock [1], concrete [2, 3] and reinforced concrete [4].

In this work a 3D rigid PM model is adopted that includes in an approximate way the polyhedral particle shape but keeps the simplicity and the reduced computational costs of rigid spherical particle models [4, 5]. The adopted VGCM-3D contact model, by enabling moment transmission and adopting a bilinear vectorial simplified softening contact model, is able to match the ratio of the compressive strength to tensile strength that occurs in a hard rock, the proper macroscopic friction angle and to give a better agreement between the direct tensile strength and the indirect tensile strength, which is not possible to obtain with the PM model proposed in [1].

In concrete, to predict a response closer to that observed experimentally a PM contact model that includes softening at the contact level may be required [2, 3]. For a brittle PM contact model to be able to predict a response closer to that observed experimentally in concrete, it is necessary to adopt a very detailed PM model that includes the heterogeneity that is present in concrete at the meso-level, greatly increasing the PM associated computational costs [7].

In concrete fracture studies a 3D PM model has been proposed that just requires the larger aggregate particles to be included in the PM model and adopts a softening/hardening contact constitutive law based on the concept of stress-strain boundary [8]. An elasto-plastic base interface contact model has also been proposed for zero-thickness interface finite elements, which also considers that concrete can be represented by the larger aggregate sizes embedded in a matrix phase using 3D finite element technology [9].

In this work the performance of the constitutive contact models [2, 8, 9] is initially compared in tensile, pure shear and compression/shear tests of a single contact. Additionally, compression, direct tensile and confined triaxial tests of quasi-brittle material discretized with spherical particles are presented and the predicted macroscopic response of the different constitutive models is compared. It is shown that the macroscopic response predicted with the three different contact models can be slightly different from each other for similar contact properties, whereas a very similar behaviour is predicted for a single contact model. The way the contact model handles the damage evolution under tensile/shear or compression/shear strongly influences the overall macroscopic response.

2 PARTICE MODEL (PM)

2.1 Voronoi-generalized contact model (VGCM-3D)

In the adopted 3D Voronoi-generalized contact model (VGCM-3D) [5, 6], the contact surface and the contact point location are defined by the Voronoi tessellation of the spherical particles gravity centers, Figure 1. The common Voronoi facet is the contact surface and the vertexes of the Voronoi facet including the gravity centre of the Voronoi facet are considered to be the local contact points locations, Figure 1. By incorporating the VGCM-3D contact model, the PM model takes into account the polyhedral shaped particles in an approximate way, but still keeps the simplicity of spherical particle models and does not require a significant increase in the computational effort.

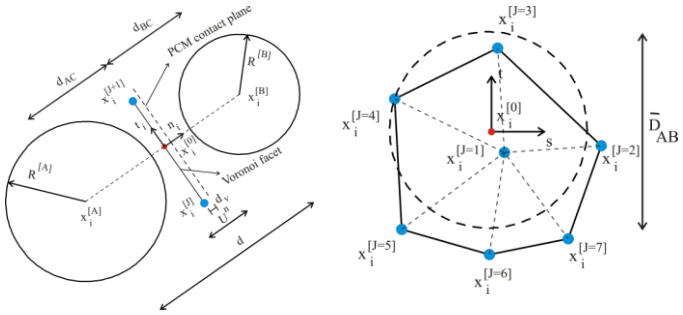

a) (t, n) plane b) (t, s) plane

Figure 1: VGCM-3D contact model with variable number of local points given by the Voronoi facet vertexes and its gravity centre

Given the normal ($k_n^{[J]}$) and shear stiffness ($k_s^{[J]}$) of each local contact point, the normal and shear forces increments are obtained following an incremental linear law:

$$\Delta F^{[J,N]} = -k_n^{[J]} \Delta x^{[J,N]} = -k_n^{[J]} \left(\dot{x}_i^{[J]} \Delta t \right) n_i \tag{1}$$

$$\Delta F_i^{[J,S]} = -k_s^{[J]} \Delta x_i^{[J,S]} = -k_s^{[J]} \left(\dot{x}_i^{[J]} \Delta t \right) - \Delta x^{[J,N]} n_i \tag{2}$$

where $\Delta x^{[J,N]}$ is the contact displacement normal increment stored as a scalar, $\Delta x_i^{[J,S]}$ is the contact shear displacement increment stored as a vector and n_i is the contact unit normal.

2.2 Local contact stiffness and local contact strength

The VGCM-3D contact stiffness is defined based on the Young's modulus of the equivalent continuum material ($\bar{E}$) and on a constant that relates the normal and the shear stiffness spring value (α):

$$k_n^{[J]} = \frac{\bar{E}}{d} A_c^{[J]} \tag{3}$$

$$k_s^{[J]} = \alpha \, k_n^{[J]} \tag{4}$$

where, $A_c^{[J]}$ is the contact area associated with the local point j and d is the distance between the particles centre of gravity. The contact strength properties are defined based on the maximum contact tensile stress ($\sigma_{n.t}$)), the maximum contact cohesion stress (τ) and the local contact point area:

$$F_{n.max}^{[J]} = \sigma_{n.t} \, A_c^{[J]} \tag{5}$$

$$C_{max}^{[J]} = \tau \, A_c^{[J]} \tag{6}$$

2.3 Bilinear softening models

2.3.1 Vectorial bilinear weakening model (BL)

A bilinear softening damage model, Figure 2, can be adopted for the contact in the normal and shear directions [2, 3, 4]. Given the current total contact damage the maximum values of tensile and cohesive strength are reduced accordingly. The contact damage is given in an approximate way by the sum of tensile and shear damage. In each direction, the damage value is defined as a function of the maximum contact displacement in that direction.

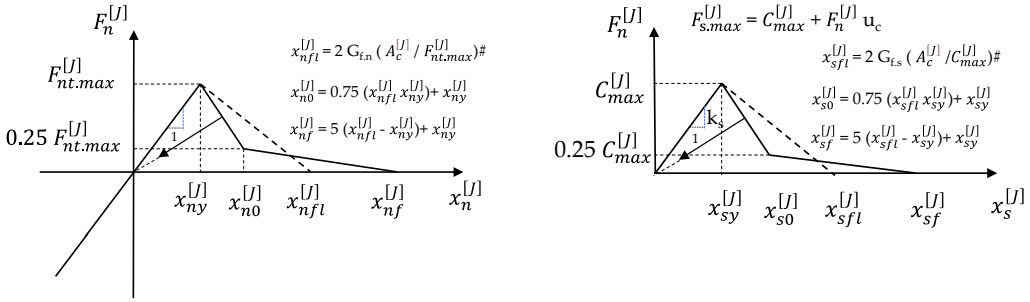

a) Normal direction b) Shear direction

Figure 2: Bilinear softening under tension and shear contact constitutive model

2.3.2 Microplane based model (MCP)

It is also possible to adopt a contact constitutive model based on the concept of stress-strain boundary proposed in the framework of 3D PM models for concrete fracture [8]. The contact model is based on a single stress-strain boundary, introducing the concept of equivalent stress, σ_{eq}, given by:

$$\sigma_{eq} = \sqrt{\left(\sigma_n^J\right)^2 + \frac{(\tau_s{}^J)^2}{\alpha}} \tag{7}$$

The local point normal contact stress, σ_n^J, and the local point contact shear stress, $\tau_s{}^J$, are given as a function of the normal force, $F_{n.}^{[J]}$, of the shear force, $F_s^{[J]}$, and of the area of the contact, $A_c^{[J]}$. The equivalent stress-strain boundary allows the simulation of weakening and hardening as a function of the equivalent contact stress state. This boundary is defined in terms of the effective strain, ε, and the coupling variable, ω, and is represented by the function:

$$\sigma_b(\varepsilon,\omega) = \sigma_0(\omega)\exp\left\{\frac{K(\omega)}{\sigma_0(\omega)}\langle\varepsilon_1(\varepsilon,\omega) - \varepsilon_0(\varepsilon,\omega)\rangle\right\} \tag{8}$$

where the value of the difference $\langle\varepsilon_1(\varepsilon,\omega) - \varepsilon_0(\varepsilon,\omega)\rangle = \max\{\varepsilon_1(\varepsilon,\omega) - \varepsilon_0(\varepsilon,\omega), 0\}\}$. The function $\varepsilon_0(\varepsilon,\omega)$ represents the limit of deformation where the boundary is no longer equal to $\sigma_0(\omega)$ but has changed exponentially as a function of $\varepsilon_1(\varepsilon,\omega) - \varepsilon_0(\varepsilon,\omega)$. The effective strain (ε) is obtained from the expression:

$$\varepsilon = \sqrt{(\varepsilon_n{}^J)^2 + \alpha\,(\varepsilon_s{}^J)^2} \tag{9}$$

where the effective normal strain, $\varepsilon_n{}^J$, and tangential strain, $\varepsilon_s{}^J$, are obtained from the normal displacement, $x_n{}^J$, and tangential displacement, $x_s{}^J$, and the inter-particle distance, d:

$$\varepsilon_n{}^J = \frac{x_n{}^J}{d} \;\&\; \varepsilon_s{}^J = \frac{\|x_s{}^J\|}{d} \tag{10}$$

Figure 3 shows the function $\sigma_0(\omega)$, which represents the boundary in the (σ,τ_s) plane, and is translated as:

$$\sigma_0(\omega) = \begin{cases}\sigma_{01}(\omega) & \text{if } \omega \le \omega_0\\ \sigma_{02}(\omega) & \text{if } \omega > \omega_0\end{cases} \tag{11}$$

where $\tan\omega_0 = \frac{\sigma_0}{\tau/\sqrt{\alpha}}$ corresponds to the point of intersection of the two curves, Figure 3a), and is related to the angle of internal friction of the MCP contact model. The function $\sigma_{01}(\omega)$ represents the boundary for high compressive stress states and is represented by an elliptical function equal to:

$$\left(\sigma_n^J\right)^2 + \frac{(\tau_s{}^J)^2}{\beta} = {\sigma_c}^2 \tag{12}$$

where σ_c is the maximum compressive stress at the contact. A value of β equal to 1.0 was considered in this work. The function $\sigma_{02}(\omega)$ represents the boundary for tensile/ shear and compressive/ shear stress states and is represented by a hyperbolic function, which relates the shear stress at the contact $\tau_s{}^J$, with the normal stress at the contact σ_n^J, considering:

$$\tau_s{}^J = \mu_1 \sqrt{(\sigma_n^J - \sigma_t - \sigma_a)^2 - \sigma_a{}^2} \tag{13}$$

When compared with the BL contact model, the MCP contact model allows a more complex macroscopic behaviour to be predicted with a lower particle refinement and it has been shown that it adequately represents concrete behaviour under complex loading patterns [8]. Contrary to the BL contact model, the MCP model adopts stress boundary for high contact compression values and the contact friction angle is an internal variable of the MCP model, Figure 3a). The interaction between the shear and normal directions is handled through the concept of equivalent stress.

2.3.3 Contact model based on plasticity theory (EP)

In a PM model in which concrete is represented by the larger aggregate sizes embedded in a matrix phase using 3D finite element technology [9], a contact model has also been proposed, in which cracking is defined based on a hyperbolic function, that allows a smooth transition from tensile cracking to shear cracking, representing the yield surface, defined in terms of the maximum tensile stress, cohesion and a frictional term:

$$F\{\sigma, \Phi\} = (\tau_s{}^J)^2 - \left(\tau - \sigma_n^J \mu_c\right)^2 + (\tau - \sigma_{n.t}\, \mu_c)^2 = 0 \tag{14}$$

The plasticity function is also a hyperbolic function, which depends on an apparent cohesion term (τ_Q) and an apparent friction term (μ_{cQ}), corresponding to a non-associated formulation:

$$Q\{\sigma, \Psi\} = \left(\tau_Q - \sigma_{n.t}\, \mu_{cQ}\right) + \sqrt[2]{(\tau_s{}^J)^2 + \left(\tau_Q - \sigma_{n.t}\, \mu_{cQ}\right)^2} = 0 \tag{15}$$

The evolution of this surface is controlled by an internal variable (W_{CR}) which is a function of the work done during the fracture process.

$$d\, W_{CR} = \begin{cases} \sigma_n^J dx_{n.crack}{}^{\mathrm{J}} & \sigma_n^J \geq 0 \quad (tension) \\ (\tau_s{}^J + \sigma_n^J \mu_c) d\|x_{s.crack}{}^{\mathrm{J}}\| & \sigma_n^J < 0 \quad (compression) \end{cases} \tag{16}$$

The maximum tensile stress, cohesion and frictional term evolution laws are controlled by the internal variable (W_{CR}) and the values of the fracture energy in mode I ($G_{f.n}$) and mode II ($G_{f.s}$). The details of the implementation of the EP model can be found in [9]. The EP contact model, like the MCP contact model, allows a more complex macroscopic behaviour to be predicted with a lower particle refinement when compared to the BL contact model. Contrary to the BP and MCP contact models, the EP model allows dilatancy to occur at the contact level and the maximum shear strength under pure shear is lower than the adopted maximum shear strength, Figure 3b). The EP contact model also requires the integration of constitutive equations that may not converge, whereas the BL contact model and in the MCP contact model are just based on analytical expressions. The EP contact model also incorporates a degradation of the frictional term which is not considered on the other models. and when non associated plasticity is adopted it has, when compared with the BL and MCP contact models, a much

higher number of unknowns that need to be calibrated.

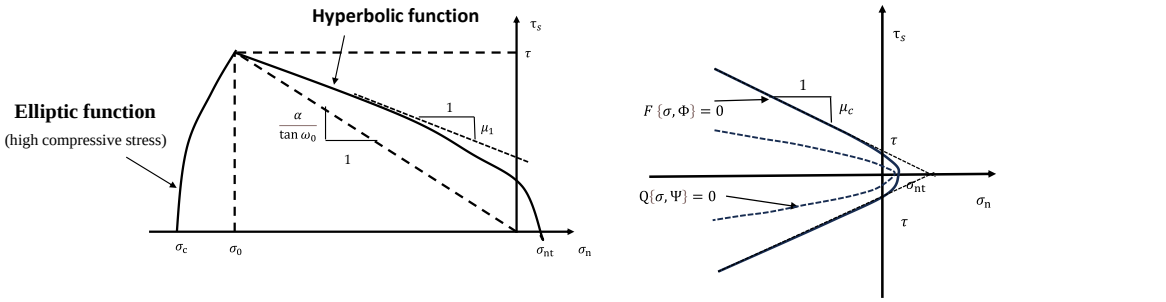

a) Microplane based constitutive model (MCP) b) Elasto-plastic based model loading surface and plastic potential (EP)

Figure 3: Microplane based constitutive model (MCP) and Elasto-plastic based model (EP)

4 CASE STUDIES

4.1 Single particle/particle contact

The performance of the constitutive contact models is initially compared in simple tensile tests (T) and in shear tests with an initial axial stress for a single VGCM3D contact, Figure 4. The adopted contact properties under tensile (T) and shear tests (S&A) are defined in Table 1 and are similar to the values adopted in [9] where the EP contact model based on plasticity theory is presented.

a) Tensile test (T) b) Shear test with axial force (S&A)

Figure 4: Single particle/particle test loading configurations

Figure 5 shows the tensile test stress-displacement curve for two different values of contact energy in mode I. As shown, a higher contact fracture energy leads to a more ductile response. The BL contact model approximates reasonably well the more complex response predicted with the EP and MCP contact models, in which the softening branch is closer to an exponential.

Table 1 – VGCM3D single contact elastic and strength properties

	$\bar{E}$ (GPa)	α	μ_c	$\sigma_{n.t}$ (MPa)	τ (MPa)	$G_{f.n}$ $[N/mm]$	$G_{f.s}$ $[N/mm]$	μ_{cr}	τ_Q (MPa)	μ_{cQ}
T	6.0	1.0	0.8	3.0	14.0	0.01 & 0.05	0.1	0.2	-	-
S&A	112.5	1.0	0.8	3.0	4.5	0.03	0.07	0.2	45.0	0.04

Figure 6 shows the shear test stress-displacement curve for four different axial stress values. The numerical predictions obtained with the different contact models in pure shear, Figure 6b)

and with low axial stress values, Figures 6a) and 6c), follow the trends observed in the tensile test, Figure 5.

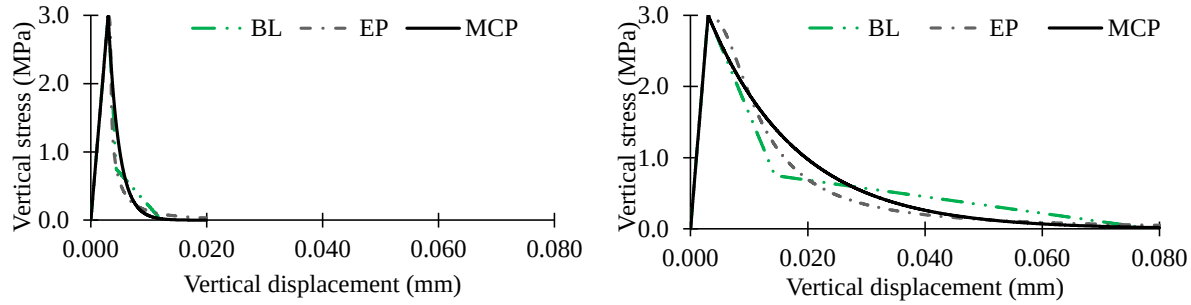

a) $G_{f.n} = 0.01\ N/mm$ b) $G_{f.n} = 0.01\ N/mm$

Figure 5: Single contact - Tensile stress vs displacement for different values of $G_{f.n}$

When compared with the BL and MCP models which adopt a constant frictional term, the EP contact model, by adopting a residual frictional angle term, allows a more complex response, Figure 6d). As shown in Figure 6d), in the MCP contact model the frictional term is an internal variable that depends on the normal and shear stiffness spring value and on the value of $\tan \omega_0$, Figure 3a). For the shear test example, and for an adopted uniaxial contact compression strength of 43.2 MPa, the internal frictional term of the MCP contact model is 0.97. As shown in Figure 6 in pure shear, Figure 6b) the maximum strength in the EP model is lower than the maximum shear strength predicted with the BL and MCP models that match the input strength value.

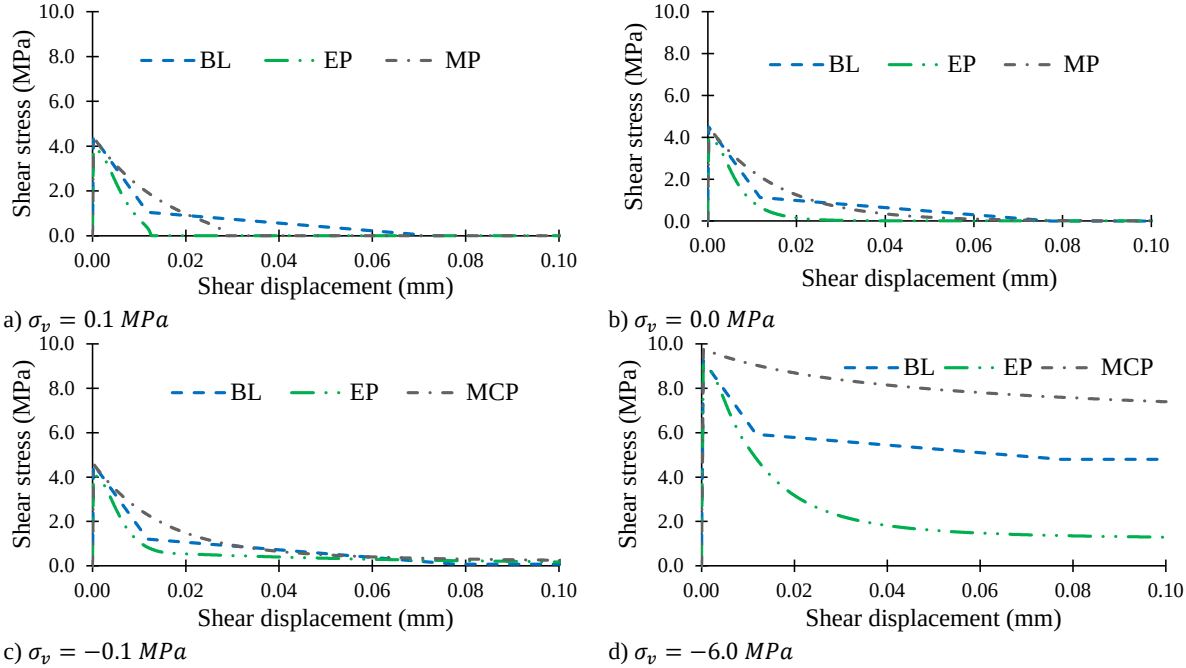

a) $\sigma_v = 0.1\ MPa$ b) $\sigma_v = 0.0\ MPa$

c) $\sigma_v = -0.1\ MPa$ d) $\sigma_v = -6.0\ MPa$

Figure 6: Single contact – Shear test under constant axial stress vs shear displacement for different values of axial stress (σ_v)

4.2 Triaxial tests in a granite rock

The numerical uniaxial tests and the triaxial tests with lateral confinement pressure are performed in cylindrical specimens with a diameter of 80 mm and a height of 160 mm, Figure 7. A uniform diameter distribution ranging from 6.0 to 9.0 mm was adopted, slightly higher than the coarse grain of distribution of an Augig granite [10]. The uniaxial and triaxial tests assemblies have on average 3000 particles with a total of 19420 VGCM3D contacts that correspond to a total of 121304 local contacts, Figure 7. An equivalent continuum material ($\bar{E}$) of 44.4 GPa and a shear and normal stiffness spring value (α) of 0.12 are the best fit contact elastic properties that predict a macroscopic Young´s modulus of 25.8 GPa and a macroscopic Poisson coefficient of 0.23 similar to the known Augig granite values [10].

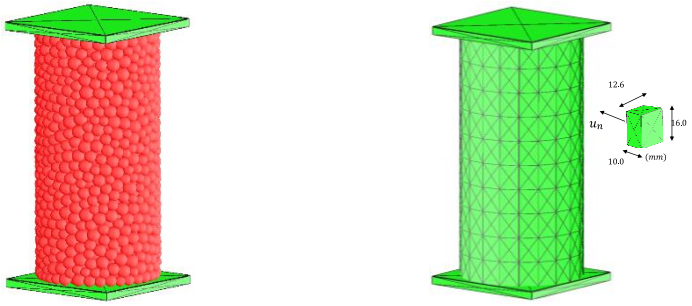

a) Uniaxial test (tensile and compression) b) Triaxial test

Figure 7: VGCM3D Granite Rock PM model

Table 2 presents the calibrated contact properties for each adopted contact constitutive model. Figure 8a) shows the predicted strength envelope for each contact model when adopting the best fit BL contact properties. Figure 8b) shows the predicted strength envelope for the best fit calibrated contact properties. As shown in Figure 8a) the EP contact model adopting the best fit BL contact properties predicts a similar macroscopic friction angle and a much lower contact uniaxial compressive and triaxial strength values. With the MCP contact model following the best fit BL contact properties a higher uniaxial compression and triaxial strength values are predicted. The MCP model also predicts a much higher macroscopic friction angle.

Table 2 – Granite Rock – Calibrated VGCM3D contact properties

	μ_c	$\sigma_{n.t}$ (MPa)	τ (MPa)	$G_{f.n}$ $[N/mm]$	$G_{f.s}$ $[N/mm]$	μ_{cr}	τ_Q (MPa)	μ_{cQ}	σ_c (MPa)
BL	0.05	14.0	77.0	0.07	21.0	-	-	-	-
EP	0.10	14.0	395.0	0.07	70.0	0.05	5925.0	0.04	-
MCP	-	13.8	35.0	0.06	18.0	-	-	-	105.0×10^3

Figure 8b) shows the strength envelopes numerically predicted with the best fit contact properties for each adopted constitutive model. As shown, with an EP contact model it is possible to obtain a good agreement with the observed experimental behaviour, namely the uniaxial compression to tensile ratio, the macroscopic cohesion and the macroscopic friction angle. With the MCP contact model the predicted macroscopic friction angle (≈ 61º) is slightly higher than the observed experimental value (≈ 48º). With the MCP value it is necessary to adopt a uniaxial contact compression strength of around 200 MPa in order to further reduce the

macroscopic friction angle, but with a maximum contact compression strength, the predicted stress-displacement response is much more ductile than the observed experimentally in a hard rock [10].

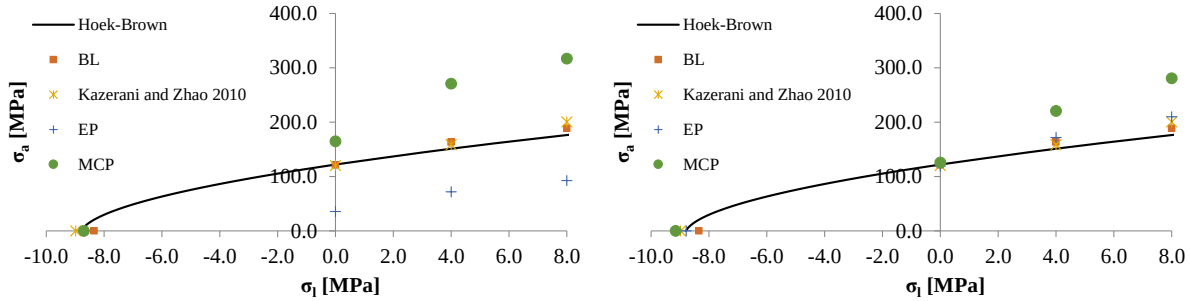

a) BL best fit parameters b) BL, EP, MCP best fit parameters

Figure 8: Granite Rock Strength Envelope

Figure 9 shows the axial stress-displacement response under uniaxial compression, Figure 9a), and for a confinement stress of 4.0 MP, Figure 9b). As shown, the numerical response predicted under uniaxial compression is within the same range for the different contact models, but for a higher confinement values the peak axial strength value predicted with the MCP model is higher and the overall response is less brittle.

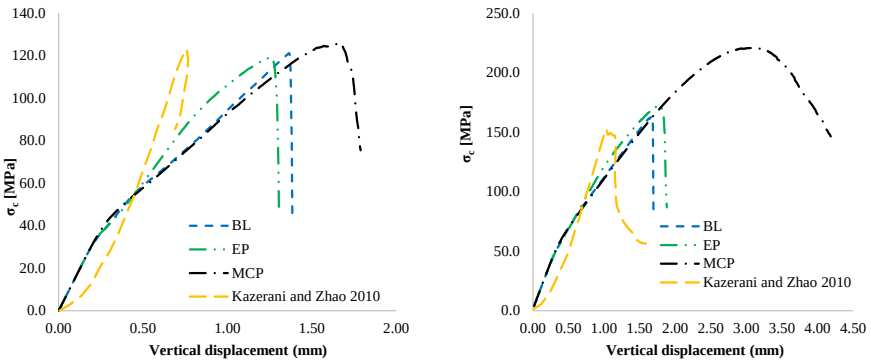

a) $\sigma_{conf} = 0.0$ MPa b) $\sigma_{conf} = 4.0$ MPa

Figure 9: Vertical stress-strain curves for the different confinement pressures

4.2 Concrete uniaxial tests

The tensile tests are carried out in a 50x100x100 mm geometry, and the compression tests are carried out in a 100x100x100 geometry. The aggregate content with dimensions ranging from 4.0 to 8.0 mm and from 8.0 to 16.0 mm, corresponding to 44 % of the total volume of the aggregate size distribution, is taken directly into consideration in the adopted PM models [11]. For the particles representing the cement paste a uniform distribution of particles with a diameter between 4.0 and 6.0 mm and a porosity of 0.1 is adopted in order to fill the void space. In the compression uniaxial tests assemblies have on average 1100 particles representing the aggregates and 8800 particles representing the cement paste, corresponding to a total of 60000 VGCM3D contacts that correspond to a total of 360600 local contacts, Figure 10.

Table 2 presents the calibrated strength contact properties for the BL contact constitutive

model and the elastic strength contact properties that predict a macroscopic Young's modulus of 32.0 GPa and a macroscopic Poisson coefficient of 0.19, that are similar to the concrete elastic properties adopted in [11]. As shown, similar contact properties are adopted for the aggregate to aggregate (A-A) contacts and for the aggregate to cement paste (A-M) contacts.

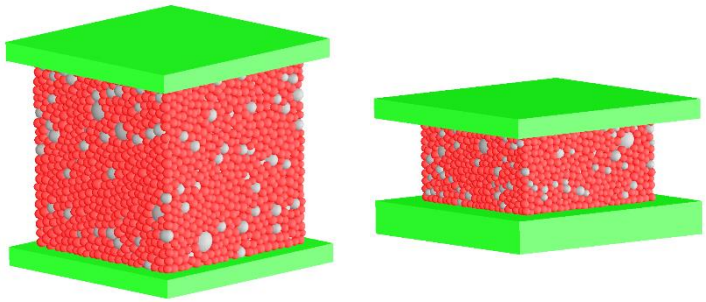

a) Compression test b) Tensile test

Figure 10: VGCM3D Concrete PM model

Table 3 – Concrete – Elastic and strength BL calibrated VGCM3D contact properties

	$\bar{E}$ (GPa)	α	μ_c	$\sigma_{n.t}$ (MPa)	τ (MPa)	$G_{f.n}$ $[N/mm]$	$G_{f.s}$ $[N/mm]$
A-A & A-M	67.4	0.2	0.2	6.90	20.00	0.006	1.3878
M-M	22.5	0.2	0.2	10.35	30.00	0.032	9.3312

Figure 11 shows the axial stress-displacement numerical predictions under uniaxial tensile and compression, including the numerical results predicted with a similar 2D PM model that adopts a contact model closer to the BL contact model and adopts a FE discretization of the aggregates embedded in a cement paste matrix [11]. As shown in Figure 11, with the BL best fit contact parameters, the uniaxial predicted response with the EP and MCP contact models is very similar to the response predicted with the BL contact model. This is because in a PM model tensile test, the contacts where damage occurs are mainly perpendicular to the load direction, and for this reason the contact stress state at these contacts is closer to a pure tensile loading.

Figure 11b) shows that the response predicted under uniaxial compression with the different contact models, when compared to the tensile test, is more differentiated. With the EP contact model, the maximum axial compression stress is much lower than the value predicted with the BP model, which is due to the maximum shear strength given as input is not the maximum shear strength under pure shear, or for tensile or low compression contact forces. The MCP contact model predicts under compression state a maximum strength much higher than the response predicted with a BL contact. This may be related to the way the contact shear force and the contact normal force are considered to interact and how the equivalent effective stress affects the stress-boundary evolution. Figure 11b) shows that when compared with the BL contact model, the MCP model requires a lower ratio of the maximum tensile to maximum shear contact strength, a similar behaviour was found to occur for a hard rock, see Table 2. Under uniaxial compression, the MCP contact model has an associated time step run cost 40% higher than the BL associated computational cost and an associated time step run cost 5% lower than the EP contact model associated computational cost.

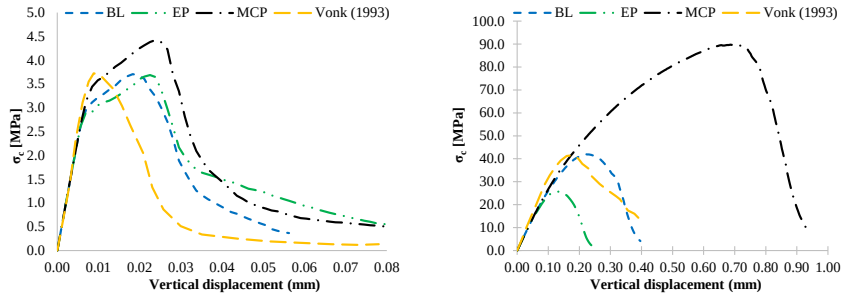

a) Tensile test b) Compression test

Figure 11: Vertical stress-strain curves for the tensile and compression test

12 CONCLUSIONS

In this work the performance of different constitutive contact models that allow softening at the contact level is compared adopting a 3D rigid PM model that includes in an approximate way the polyhedral particle shape but keeps the simplicity and the reduced computational costs of rigid spherical particle models.

It is shown that for a single contact point under tensile, pure shear and shear under constant axial force, the contact models response has some similarities. It is also shown that for higher axial forces the differences in the predicted responses are more noticeable.

In the triaxial tests of a granite rock that were carried out it is shown that it is possible to predict the experimental hard rock behavior with the BL and with the EP contact models. With the MCP contact model the predicted macroscopic friction angle is higher than the value observed experimentally even for a low value of contact friction. It would be possible to predict a similar macroscopic friction angle with a MCP contact model if a particle assembly with a lower coordination number was adopted.

The axial tensile tests and compression tests on concrete specimens show that with the BL best fit contact parameters the uniaxial tensile predicted response with the EP and MCP contact models is very similar to the response predicted with the BL contact model. This is due to the fact that in a tensile test the contacts where damage occurs are mainly perpendicular to the load direction, and for this reason the contact stress state is closer to a pure tensile state. The response predicted under uniaxial compression with the different models has more noticeable differences. With the EP contact model, the maximum axial compression stress is much lower than the value predicted with the BP model, which is due to the fact that the maximum shear strength given as input is not the maximum shear strength under pure shear, or for tensile or low compression contact forces. The MCP contact model predicts under a compression state a maximum strength much higher than the response predicted with a BL contact which may be related to the way the contact shear force and normal force are considered to interact and how this parameter affects the stress-boundary evolution.

As shown, it is possible to calibrate the three contact models in order to make them reproduce complex macroscopic behaviour. Under compression, the MCP contact model tends to predict a less brittle behaviour when compared with other models and for rock fracture it may require a particle assembly with a lower coordination number. The BL contact model is shown to be

more suitable to use in detailed PM models due to the lower associated computational costs and to the lower number of associated contact parameters that need to be calibrated.

ACKNOWLEDGMENTS

The authors thank the Portuguese Foundation for Science and Technology (FCT) for funding the Project "Seismic and Structural Health Monitoring for Large Concrete Dams (SSHM4Dams)", PTDC/ECI-EGC/5332/2020.

REFERENCES

[1] Potyondy, D. and Cundall, P. A bonded-particle model for rock. *International Journal of Rock Mechanics & Mining Sciences* (2004) **41**(8): 1329-1364.

[2] Monteiro Azevedo, N. A rigid particle discrete element model for the fracture analysis of plane and reinforced concrete. *Phd Thesis*, Heriot-Watt University, Scotland (2003).

[3] Monteiro Azevedo, N., Lemos, J.V. Aggregate shape influence in the fracture behaviour of concrete. *Structural Engineering and Mechanics* (2006) **24**(4): 411-427.

[4] Monteiro Azevedo, N, Lemos, JV, Almeida J. A discrete particle model for reinforced concrete fracture analysis. *Structural Engineering and Mechanics* (2010) **36** (3): 343-361.

[5] Candeias, M., Monteiro Azevedo, N., Farinha, L. A 3D particle model for rock fracture based on the Voronoi diagrams of the granular structure, *Geotecnia* (2018) **143**:171-197 (in Portuguese).

[6] Candeias, M., Monteiro Azevedo, N., Farinha, L., VGCM3D – A 3D rigid particle model for rock fracture following the Voronoi tessellation of the grain structure: Formulation and Validation, Proceedings of the V International Conference on Particle-Based Methods Fundamentals and Applications, September 2017, Hannover.

[7] Suchorzewski, J., Tejchman, J. and Nitka, M. Discrete element method simulations of fracture in concrete under uniaxial compression based on its real internal structure, *International Journal of Damage Mechanics* (2018) **27**(4):578-607.

[8] Cusatis, G., Bazant, Z. and Cedolin, L. Confinement-shear lattice model for concrete damage in tension and compression, *Journal of Engineering Mechanics* (2003) 129 (12), 1439-1448.

[9] Caballero, A., William, K.J. and Carol, I. Consistent tangent formulation for 3D interface modelling of cracking/fracture in quasi-brittle materials, *Computer Methods in Applied Mechanics and Engineering* (2008) **197**:2804-2822.

[10] Kazerani, T. and Zhao, J. Micromechanical parameters in bonded particle method for modelling of brittle material failure, *International Journal for Numerical and Analytical Methods in Geomechanics* (2010) **34**(18):1877-1895.

[11] Vonk, R. A micromechanical investigation of softening of concrete loaded in compression, *Heron* (1993) **38**(3): 1-94.